Egyptian Journal of Chemistry

http://ejchem.journals.ekb.eg/

Fabrication and Characterization of Functionally Graded Nanomaterials (Al/Al$_2$O$_3$) and (Al/Ni/Al$_2$O$_3$) using the Sputtering Technique

Engy M. Sadek[a], Lamiaa Z. Mohamed[b,*], Emad F. El-Kashif[a], Aliaa Abdelfatah[b]

[a] Department of Mechanical Design and Production, Faculty of Engineering, Cairo University, 12613, Egypt.
[b] Mining, Petroleum, and Metallurgical Engineering Department, Faculty of Engineering, Cairo University, 12613, Egypt.

Abstract

Two aluminum functionally graded nanomaterials (FGNMs), sustainable and echo-environmentally friendly, Al/Al$_2$O$_3$ (AA) and Al/Ni/Al$_2$O$_3$ (ANA), were fabricated by magnetron sputtering technique on an Al substrate. The properties were characterized using XRD, SEM, EDX, mapping for elemental distribution, AFM, FTIR, and spectrophotometer. Also, the nanoindentation (NIN), electrochemical behavior in 3.5%NaCl, and the wettability test were studied. The SEM micrographs show a homogenous layer for both AA-FGNM and ANA-FGNM. The sustainable solar cell material AA-FGNM has high nano-hardness. It is hydrophobic, whereas ANA-FGNM is hydrophilic. The AA-FGNM provides a high selectivity (absorbance/emittance (α/ε)) of 0.967/0.18, contrasted to 0.943/0.32 for the ANA-FGNM. This combination of properties makes AA-FGNM a good candidate for solar cell and mechanical applications due to its low nanoindentation, whereas ANA-FGNM is a good candidate for marine applications due to good corrosion resistance. The ANA-FGNM offers superior corrosion resistance in 3.5% NaCl, which has the lowest corrosion rate (0.005 mm/y) as compared with the AA-FGNM deposited layer.

Keywords: Function graded materials; Magnetron sputtering; Optical properties; Nanolayer deposition; Nanoindentation.

1. Introduction

Function-graded materials (FGMs) are innovative, sophisticated materials having variable qualities along changing dimensions [1, 2]. The FGMs eliminate the abrupt interfaces that trigger failure in composite materials. It substitutes this strong contact with a gradient interface, resulting in a seamless transition between materials [3, 4]. Numerous applications, including automotive, aerospace, microelectronics, power generation, structural, and bioengineering, need engineered materials with unobtainable features [5, 6, 7]. FGM is distinguished by its ability to customize materials to purposes [4].

Several investigations on graded nanocomposites have been conducted [1].

Historically, surface treatment procedures were used to achieve the desired qualities. However, there were always issues with the interface characteristics and surface film adherence to the substrate materials [8]. Moreover, the deposited surface film might not be adequate to provide the desired product durability [9]. Alloying may be done to partly enhance performance, such as when it is difficult or impossible to alloy two materials with vastly different melting temperatures except if the material is laminated with uniformly distributed [10]. Although laminated composites may create narrow but distinct characteristics that vary throughout the thickness, they are susceptible to interlaminar shear stresses and discontinuities [5]. Six traditional classification criteria were proposed to categorize FGMs based on processing status, FGM structure, nature of FGM gradient, FGM type, principal dimensions, and application area [11, 12]. FGM fabrication processes contain lamination, powder metallurgy, chemical vapor deposition (CVD) and physical vapor deposition (PVD), centrifugal casting, and infiltration, as well as the additive manufacturing (AM) or solid freeform fabrication (SFF) family with its subclasses [5].

Numerous articles [13] detail the specifics of the various manufacturing processes and examine their technicalities, benefits, limits, applications, and research trends. Thermal spray deposition [14], PVD [15], CVD [16, 17], and laser cladding [18, 19, 20] are used to create thin FGMs. Thin FGMs vary between 5 nm and 500 nm [21, 22] and might be expanded to the micrometer range (for instance, 1–120 μm thick deposited films [15, 23]. Al oxide and nitrides are gaining prominence due to their crucial optical characteristics; they may also be produced directly by sputtering or oxidation [24].

Wettability is an essential feature for measuring the coating performance. Generally, the coating must have a certain wettability based on its intended use. In an ice-free environment, for instance, hydrophobic coatings are required to reject atmospheric water droplets; in the oil–water separation test, the coating must have differing oil and water wettability [25]. Super hydrophobic coatings used for metal protection have shown various desired qualities, such as corrosion resistance (CRST) [26, 27, 28]. A similar study [29, 30, 31, 32] has proven that the hydrophobicity of a surface may be increased by roughening and altering it with a low-surface-energy organic molecule. Surface features are doomed to be abrasion-vulnerable, a typical and significant issue for most superhydrophobic surfaces. Current solutions for tackling this problem depend mainly on modest improvement techniques, such as increasing mechanical hardness [33], creating a self-healing surface [34], and adopting a unique lithography structure [35], among others. Anodic aluminum oxide (AAO), which has several advantageous qualities like CRST, abrasion resistance, high hardness, and excellent functionality, has widespread use in various sectors [36, 37].

Nanoindentation (NIN) is essential for assessing composite resin's hardness and resilience [38]. This approach is crucial for determining whether a nanoscale material can be deformed or resist high pressures permanently. In addition to knowledge of chemical, biological, pathological, and physical concepts crucial to developing effective dental therapies [38, 39], the NIN approach is valuable for understanding the mechanical characteristics of dental materials. NIN is an exact, non-destructive procedure since occlusal forces are measured in the N range [40, 41]. The NIN methodology may be used with applicable software tools to determine other

parameters that are impossible with traditional techniques [39, 42]. The method primarily evaluates hardness (H) and modulus of elasticity (E), where H refers to the resistance of FGNM to penetration and indentation. E simultaneously defines a material's stretchability and relative stiffness without causing permanent deformation under continual stress [43, 44]. The NIN can assist in comprehending and describing the activities of FGNM in various operating circumstances and oral environments. NIN may also be used to characterize the composite resins' wear resistance against occlusion loads and forces based on their hardness [45].

Instrumented NIN has evolved owing to this technique's latest significant growth in numerical modeling. Bobzin et al. [46] offer a three-dimensional NIN model of coatings for tool steel. While, Khan et al. [47, 48] constructed a finite-element model of the NIN process for corrosion-resistant Al coating. The NIN approach is commonly used to assess the nanometer-scale hardness and decreased elastic modulus of materials [38]. The substitution of pure Al single layer with Al/Al_2O_3 multilayers should hinder columnar development and increase the CRST of the substrate of sintered NdFeB magnets [49].

Researchers are intensely interested in producing alumina thin films to shield substrates made of metallic and other materials. The Sol–gel deposition of a single layer of Al_2O_3 enhanced the CRST of the substrate [50, 51]. Also developed was an ultra-thin (10–100 nm) protective alumina coating deposition on a 100Cr6 steel substrate. The corrosion rate (CR) dropped by one to four orders of magnitude as the Al_2O_3 sheet's thickness grew from 10 to 100 nm, according to D'az et al [52]. Similar findings were also reported by Potts et al. [52] using the salt spray test technique. In their investigation, the CRST of thicker alumina coatings, such as 50 nm, was greater

than that of thinner coatings, such as 10 nm. On Ck45, low-carbon steel, reactive evaporation, and ion beam-assisted deposition (IBAD) procedures were used to create strong and corrosion-resistant alumina thin coatings [53, 54]. Stippich et al. [54] observed that an alumina coating with a thickness of 100 nm exhibited greater CRST; nevertheless, the critical thickness of CR was in reverse proportional to the thickness beyond this point. The CRST of the direct sputtered film was greater than that of the reactive sputtered film, which might be attributed to the increased film thickness [55]. High CRST values were observed for coated conditions relative to the base alloy, principally owing to the barrier and inert nature of micro-arc oxidation (MAO) coatings when evaluated in 3.5% NaCl [56]. Combining comparatively decreased surface roughness (Ra), a corrosion-resistant barrier coating, and favorable subsurface compressive residual stresses is optimal for protecting components from corrosion and corrosion-fatigue damage [56].

Selected solar coatings are applied to the receiver tube for excellent absorbance and low emissivity [57]. It has been reported that the $Al-Ni/Al_2O_3$ coating has a strong selectivity (absorbance/emittance (α/ε)) of 0.96/0.10 [58]. Al and Ni proposed to have FCC structures to prevent heat transfer between the substrate and Al coating. The effect of the deposited layers on the characterization is affected by different factors one of them being the substrate materials. Our previous work, the Al/Al_2O_3 thin layer has a higher selectivity (absorbance/emittance (α/ε)) (0.92/0.05) than the Ni/Al_2O_3 coating, which has a value of 0.91/0.15 on 304LSS substrate [24]. This research aims to fabricate and characterize the sustainable and echo-environmentally friendly Al/Al_2O_3-FGNM (AA-FGNM) and $Al/Ni/Al_2O_3$-FGNM (ANA-FGNM) using magnetron sputtering (radio-frequency (RF)) technique on pure Al

substrate. The X-ray diffraction (XRD), scanning electron microscope (SEM), energy dispersive X-ray analysis (EDX), mapping for elemental distribution, atomic forced microscope (AFM), Fourier transform infrared spectroscopy (FTIR), and spectrophotometer were investigated for the fabricated FGNMs. Also, the nanoindentation (NIN), electrochemical behavior in 3.5%NaCl, and the wettability test were examined.

2. Materials and Methods

Two distinct layers were deposited by sputtering under defined deposition circumstances. Fabrication of AA-FGNM and ANA-FGNM by depositing thin layers as Al_2O_3 and Ni/Al_2O_3, respectively, on Al substrate using a PROTOFEEX sputtering 1600-Magnetron 6 (USA) sputtering equipment with an extreme output power of 2.5 kW and a frequency of 13.6 MHz. The Al substrate was used 99.9% of the time. Pure Ni target (99.999%) and pure Al_2O_3 target (99.999%) of size (30x10 cm^2) were used for the deposition of all thin layers in the reactive medium employing 30 Sccm of Ar gas. The size of the Al substrates was 20x20x1 mm^3. Substrates were placed in the chamber for each run, which was cleaned with

2.1 FGNM preparation

acetone and isopropanol and then dried. They were positioned in the deposition chamber with a rotational speed of 10 rpm and a bias voltage of 150 V. Throughout the deposition, the sputtering power was maintained at 1.15 kW, and the starting vacuum pressure was 10^{-5} Pa, but the chamber base pressure was lowered to 10^{-3} Pa. During the sputtering process, the chamber (of circular shape with a 50 cm diameter) was worked at 160 °C, as shown on the digital screen, and the distance relating the substrate and the target was 10 cm. Each process deposition took about 140 min. The design of selective solar absorber (SSA) layers placed on an Al substrate is shown in Fig. 1: AA-FGNM and ANA-FGNM.
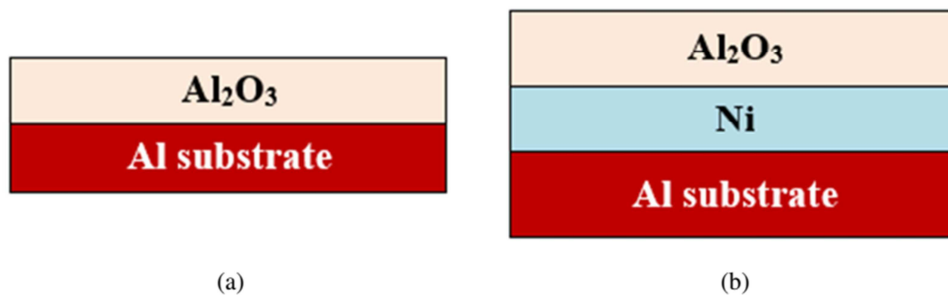

Figure 1: The SSA layers design

2.2 Morphology

The SEM (model FEI inspect S-Netherlands) and EDX were used to examine the surface morphology (SM) and cross-section of the samples (Bruker AXS-flash detector Germany). The elements distribution on the surface and cross-section of the fabricated thin layers was identified using mapping. In addition, an Agilent Technologies 5600LS AFM atomic force microscope (AFM) was employed to acquire 2D and 3D AFM images for surface morphological investigation. AFM revealed the thickness and overall roughness of the fabricated thin layer.

2.3 Phase Identification (PI)

The PI was studied using XRD (model Bruker) with scanning range $10 \leq 2\theta \leq 100°$ intervals, step size 0.1 deg, and α Cu target running at 40 kV and 30 mA. The average particle size of the coating was estimated through Debye–Scherer equation as provided in Eq. 1:

$$D = \frac{K\lambda}{\beta \cos\theta} \tag{1}$$

where "D" denotes the particle size, "k" denotes Scherer's constant (K=0.94 for spherical shape), "λ" denotes the wavelength (λ = 1.54056 Å) of X-ray radiations, "β" means the width (full-width half maxima) of XED peak in radians and "θ" denotes the Bragg angle [24, 59].

2.4 Wettability

The wetting angle has long been an essential metric for determining the wetting qualities of substances. It is mainly utilized to determine the hydrophobicity and hydrophilicity of substances. A high wetting angle indicates poor wetting capability [25].

2.4 Optical characteristics

A spectrophotometer evaluated the optical characteristics and FTIR for absorbance and emittance, respectively. FTIR is a NICOLET 6700 model where the spectrophotometer is UV-3600 from Shimadzu. The absorbance was measured in the ultra-violet (UV), visible, and near-infrared (near IR) ranges (0.2 – 2.5 µm), whereas the emittance was recorded in the long IR range (2.5-25 µm). Optical characteristics were conducted at room temperature (RT). Using Kirchoff's rule, which states that for opaque materials, absorbance $\alpha(\lambda)$ and thermal emittance $\varepsilon(\lambda)$ are equal, the requisite characteristics were estimated from the test data. Eq. (2) may be used to obtain α & ε [60] from the reflectance $R(\lambda)$:

$$\alpha(\lambda) = \varepsilon(\lambda) = 1 - R(\lambda) \tag{2}$$

The equation can express the emittance $\varepsilon(T)$ at definite temperature T (3) [24, 61]:

$$\varepsilon(T) = \frac{\int_{\lambda min}^{\lambda max}[1-R(\lambda,T)]B(\lambda,T)d\lambda}{\sigma T^4} \tag{3}$$

σ describes the Stefan–Boltzmann constant (5.6696×10^{-8} W.m^{-2}.K^{-4}).

B (λ, T) denotes blackbody spectral irradiance at λ, and T. Planck's law is employed to determine B (λ & T) as revealed in Eq. (4):

$$(\lambda, T) = \frac{C_1}{\lambda^5 [e^{(\frac{C2}{\lambda T})}-1]} \tag{4}$$

Planck's first and second constants denote c1 = 3.7405×10^8 W.µm^4.m^{-2} and c2 = 1.43879×10^4 µm. K, respectively.

2.5 Nanoindentation (NIN)

The NIN was determined to estimate the mechanical properties using the Nano Indenter® G200 device, at a loading capability of 500 mN, delivering <0.01nm (10 pm) displacement resolution and more than 500 µm maximum indentation depth and indenter travel with 0.2 pm displacement resolution.

The NIN testing, the hardness H, and the reduced elastic contact modulus $E_C^{`*}$ of investigated materials are estimated as a function of the indentation depth. The hardness is known as the load separated by the projected contact area between the indenter and the specimen [62]:

$$H = \frac{p}{A_C} \tag{5}$$

P denotes the applied load, and Ac represents the projected contact area. The A_c is calculated using a geometrical relation from the contact depth h_c.

$$A_C = \pi (\tan(\theta)h_c)^2 \tag{6}$$

Where θ denotes the equivalent angle of the conical indenter (for a Berkovich tip, θ =70.32°).

2.6 Corrosion characteristics:
2.7.1 Potentiodynamic Polarization (PDP)

The electrochemical investigation was conducted at 25 °C using a PGZ 100 Potentiostat device and a corrosion cell holding 500 ml of 3.5% NaCl at ambient temperature (RT). The open circuit potential

(OCP) was measured using a platinum auxiliary electrode and a calomel reference electrode. Each test employs a fresh specimen. The analysis of potentiodynamic polarization was conducted from -500 mV vs. OCP to +500 mV vs. OCP at a scan rate of 2 V/s, followed by the measurement of corrosion currents. From Tafel curves of potential vs. the logarithm of corrosion current density, the corrosion potential (E_{corr}) and corrosion current density (i_{corr}) are assessed. In Eq. 7 [63], the CR is determined as follows:

$$CR \ (mm/y) = (0.00327 \ x \ i_{corr} \ x \ eq.Wt)/D \qquad (7)$$

Where i_{corr} denotes the current density in mA/cm^2, D represents the density in g/cm^3; eq. wt. is the equivalent weight in grams.

3. **Results and Discussion**

3.1 Morphology

3.1.1 Surface Morphology (SM)

Fig. 2 explains the SEM and mapping results of the coated AA-FGNM. The EDX results of the surface-coated AA-FGNM in wt.% are 7%O and 93%Al. Fig. 2 illustrates the Al and O elemental distribution mapping on the Al substrate surface, indicating their good distribution over the surface. Fig. 2 confirms the successful deposition of the Al$_2$O$_3$ film on the Al substrate, which ensures the appropriateness of the deposition conditions. The Al and O show a uniform distribution on the Al substrate.
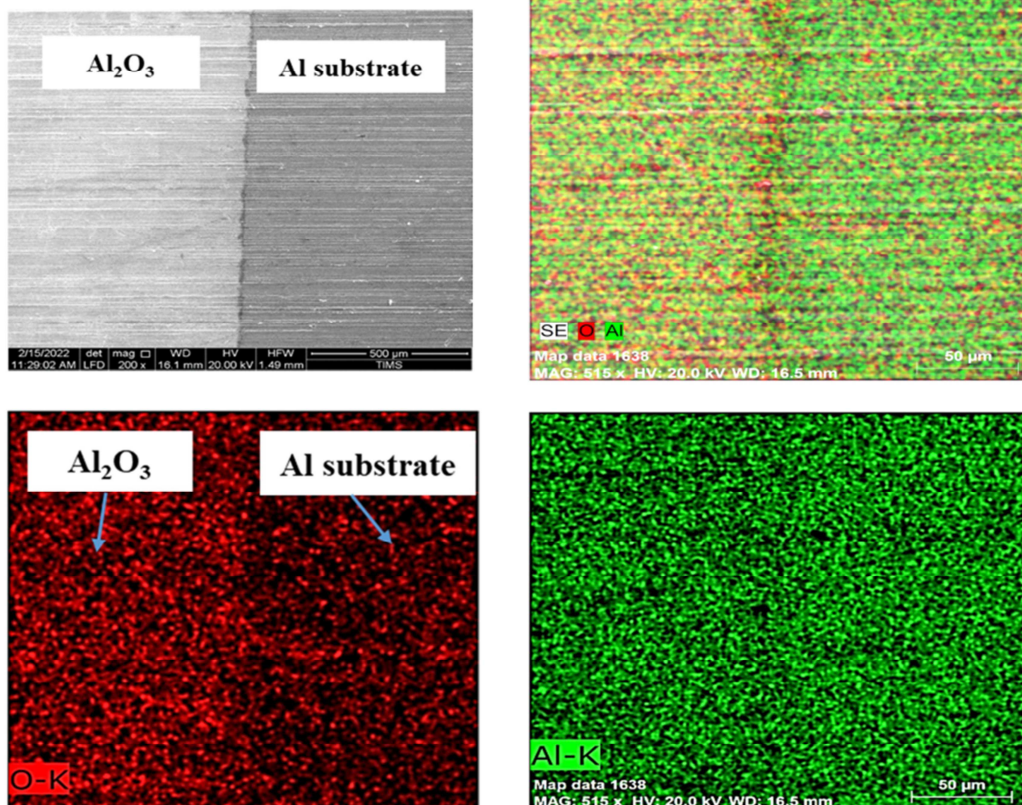

**Figure 2:** The SEM and mapping images of AA-FGNM

3.1.2 Cross-section Morphologies

Fig. 3a shows the SEM morphology and line-EDX pattern of the cross-section of AA-FGNM. Fig. 3b presents the mapping of the cross-section of AA-FGNM. The Al_2O_3 layers are cleared at the surface of the mapping. Also, Fig 4a provides the SEM micrograph and line-EDX pattern of the cross-section of ANA-FGNM, and Fig 4b gives the mapping of ANA-FGNM of the cross-section with Ni/Al_2O_3 coating layers. The mapping of the cross-section of AA-FGNM and ANA-FGNM shows a uniform distribution of the coating layers on the Al substrate. The SEM, EDX, line-EDX, and mapping were performed as evidence of the deposition of the coating layers with a good distribution along the Al substrate.
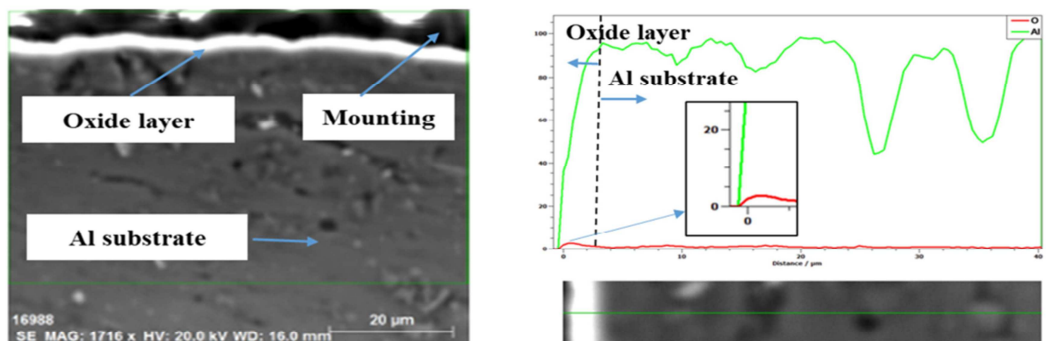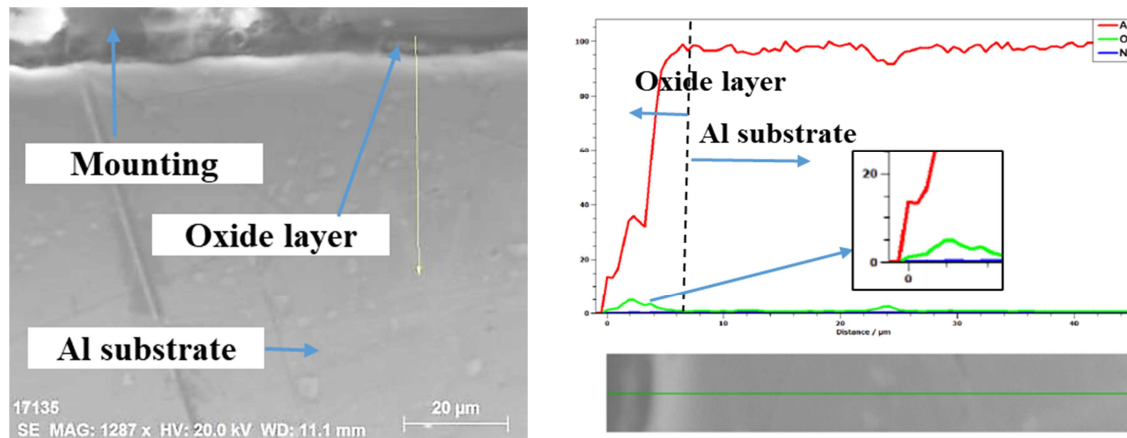

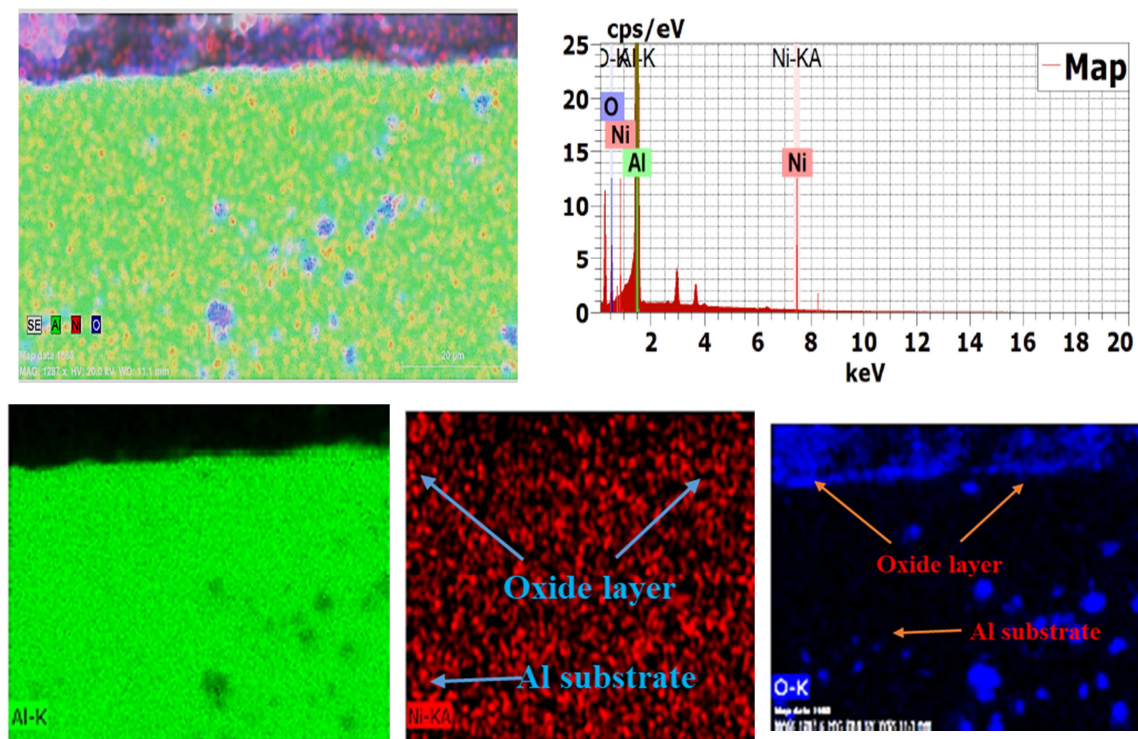(a) SEM/Line-EDX analysis of a cross-section of AA-FGNM
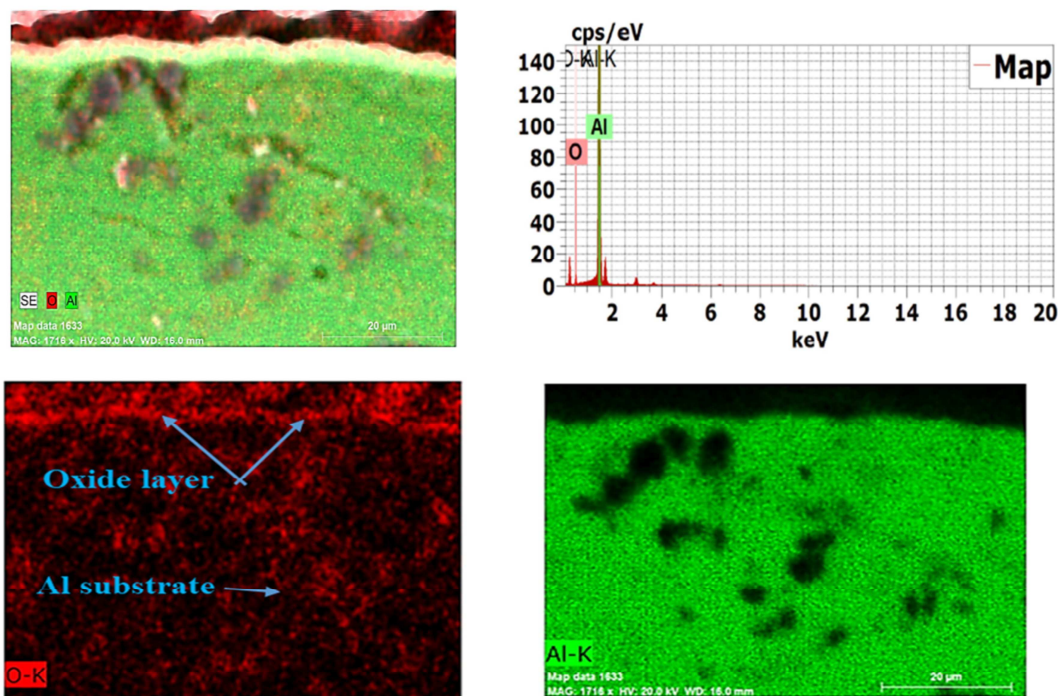
(b) Mapping of the cross-section of AA-FGNM

Figure 3: The cross-section of AA-FGNM

(a) SEM/Line-EDX analysis of a cross-section of ANA-FGNM

(b) Mapping of the cross-section of ANA-FGNM

Figure 4: The cross-section of ANA-FGNM

3.1.3   AFM study

Fig. 5 shows the 2D and 3D AFM images of the Al substrate, AA-FGNM, and ANA-FGNM. Fig. 6 provides the thickness of the deposited layers on Al substrates. The thickness values of AA-FGNM and ANA-FGNM are 200 µm and 201 µm, respectively.

The roughness of Al substrate, AA-FGNM, and ANA-FGNM surfaces are 1.33, 8.06, and 2.80 nm, respectively. After depositing thin film for AA-FGNM, the roughness of the coated surfaces increased. This raised the absorbance due to enhanced light scattering in the thin layer, as stated in

the section on optical characteristics. The deposited films of AA-FGNM and ANA-FGNM have a thickness of around 200 nm, which is suitable for selective solar applications.
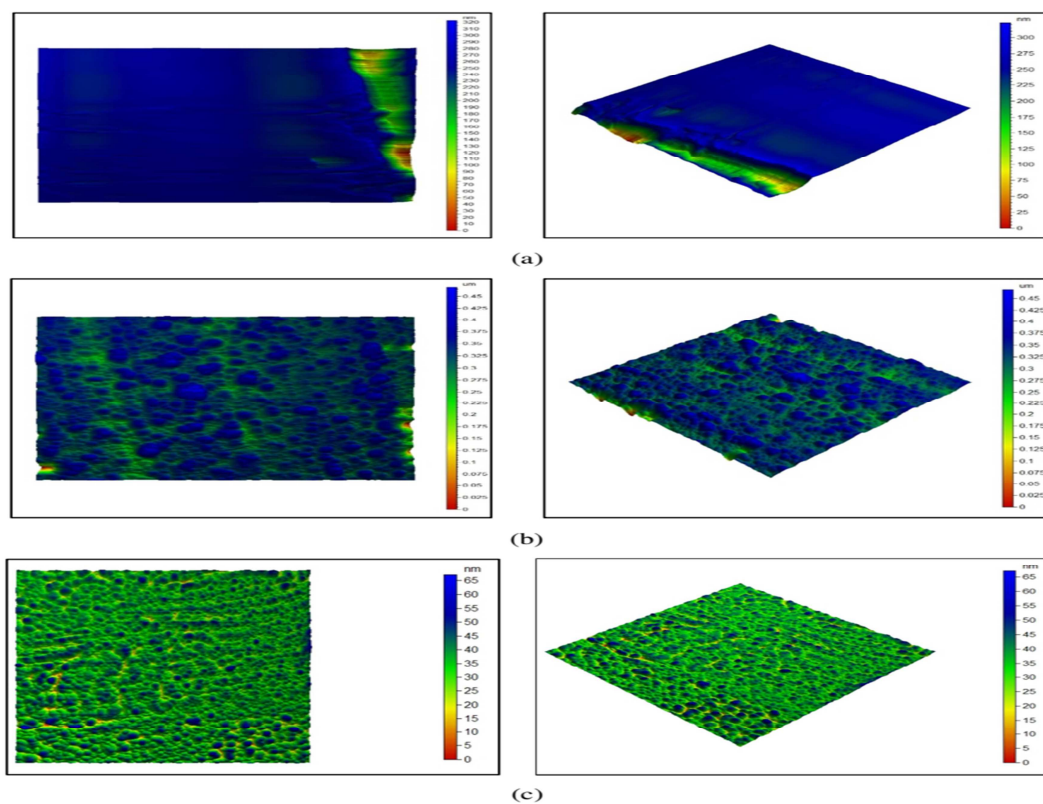

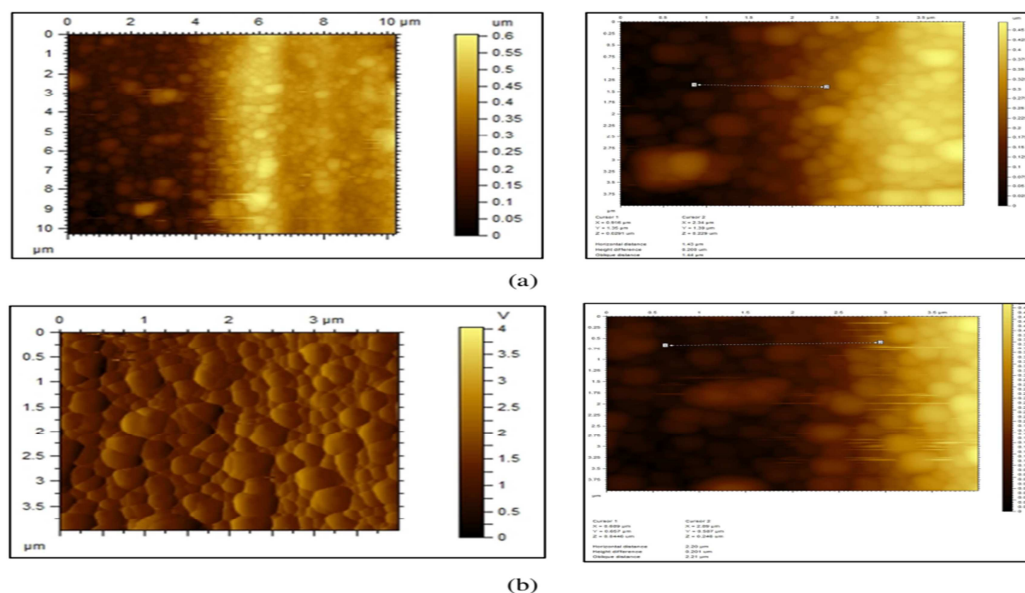**Figure 5:** AFM images 2D and 3D of (a) Al substrate, (b) AA-FGNM, and (c) ANA-FGNM

Figure 6: Thickness of deposited layers (a) AA-FGNM, and (b) ANA-FGNM

3.2   Phase Identification

The Al substrate, AA-FGNM, and ANA-FGNM patterns are shown in Fig. 7. The 2θ values of the Al substrate are $38.56°$, $44.83°$, $65.26°$, and $78.44°$. (Pattern: COD 1512488). Al_2O_3 (orthorhombic structure) has 2θ values of $38.52°$, $40.52°$, $41.67°$, $44.77°$, $65.12°$, $77.22°$, and $78.27°$ in AA-FGNM (Pattern: COD 1000442). Applied to the Debye–Scherer equation, the average particle size of Al_2O_3 is 20 nm for Al/Al_2O_3-FGNM and about 45 nm for $Al/Ni/Al_2O_3$-FGNM. In ANA-FGNM, the diffraction peaks of Ni at 2θ at $44.21°$, $51.51°$, and $75.84°$ with (Pattern: COD 2100637), and 2θ of Al_2O_3 (hexagonal structure) are $37.76°$, $41.67°$, $43.34°$, $46.16°$, $66.49°$,

and $77.22°$ with (Pattern: COD 1000017) [64, 65, 66]. Al_2O_3 in AA-FGNM has the alpha form of the Al_2O_3 orthorhombic structure. Still, the oxide layer in ANA-FGNM has the alpha form of the Al_2O_3 hexagonal structure, as shown by XRD peaks at 2θ values at $44.21°$, $51.51°$, and $75.84°$ which (Pattern: COD 2100637), and 2θ values of Al_2O_3 (hexagonal structure) are $37.76°$, $41.67°$, $43.34°$, $46.16°$, $66.49°$, and $77.22°$ (Pattern: COD 1000017) [64, 65, 66]. The XRD results show that the Al_2O_3 in AA-FGNM is the alpha form of the Al_2O_3 orthorhombic structure, while the oxide film in ANA-FGNM is the alpha form of the Al_2O_3 hexagonal structure.
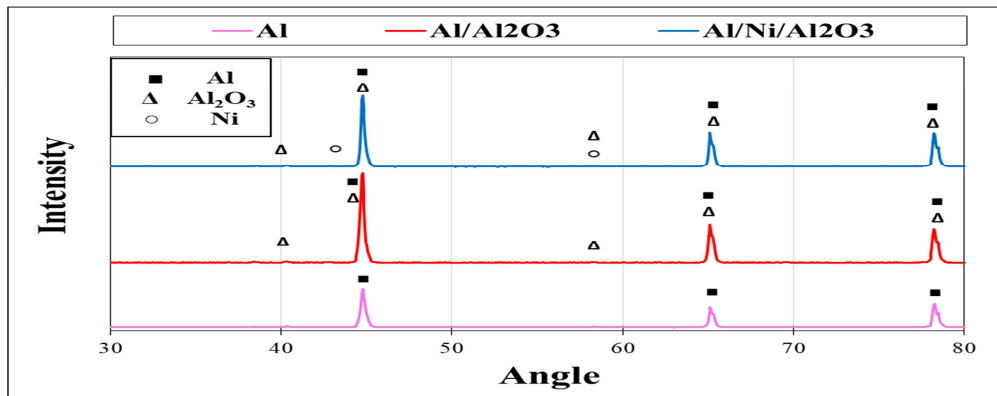

Figure 7: The XRD results of Al substrate, AA-FGNM, and ANA-FGNM

3.3   Wettability

Fig. 8 represents the contact angles of the wettability test of the Al substrate, AA-FGNM, and ANA-FGNM. The right contact angles for Al substrate,

AA-FGNM, and ANA-FGNM are $81.50°$, $106.99°$, and $86.10°$, respectively. ANA-FGNM is a hydrophilic coating, whereas AA-FGNM is a weak hydrophobic coating.
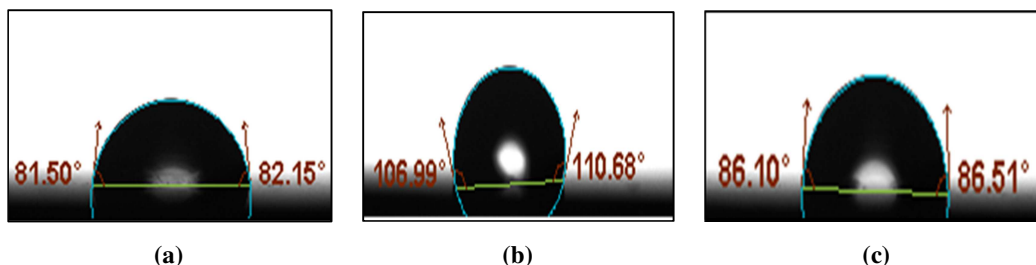

| (a) | (b) | (c) |

Figure 8: Contact angles for the wettability test of (a) Al substrate, (b) AA-FGNM, and (c) ANA-FGNM

3.4 Optical Properties

Fig. 9 shows the optical properties (absorbance% and emittance %). Fig.9(a) provides the absorbance percentage of Al substrate, AA-FGNM, and ANG-FGM vs. wavelength in nm. Fig. 9(b) gives the emittance percentage of Al substrate, AA-FGNM, and ANG-FGM vs. wavelength in nm. This is due to the restricted travel distance of the reflected light beam of the spectrophotometer, which is smaller than the thickness of the thin layer [67]. As seen in Fig. 9(a), the as-deposited thin films have more significant UV and visible light absorption. High UV and visible absorption are characterized by a particularly steep edge and metal-like behavior. D-type free electron interband transitions are referred to as the rather steep edge [68, 69]. AA-FGNM has a greater absorbance than ANA-FGNM, as seen in Fig. 9(a). Also, Fig. 9(b) gives a lower emittance percentage for AA-FGNM than ANA-FGNM. Due to increased light scattering in the thin film, AA-FGNM has the maximum roughness, which enhances its absorbance. The shadowing effect, which occurs from the preferential deposition of incoming atoms on surface protrusions, increases Ra during film formation [70]. Compared to the ANA-FGNM, the AA-FGNM exhibits superior selectivity (absorbance/emittance (α/ε) of 0.967/0.18). This combination of characteristics makes AA-FGNM an excellent choice for solar cell applications.

The AA-FGNM exhibited a rougher surface than the ANA-FGNM, resulting in greater absorbance owing to enhanced light scattering. The Al_2O_3 thin film formed in this study, with spherical crystallites ranging in size from 20 nm (10~35 nm) for AA-FGNM and about ~ 45 nm for ANA-FGNM, contributed to their selectivity performance. The diameters of the crystallites imply that the thin Al_2O_3 film formed is of the α-Al_2O_3 kind. Alpha alumina is almost impenetrable and has a small surface area [71]. The directly deposited α-Al_2O_3 in this study had an absorbance of 0.967-0.943 and an emittance of 0.18-0.32 for AA-FGNM and ANA-FGNM, respectively. Al/Al_2O_3 on 304LSS thin films had an absorbance of 91.6% and an emittance of 0.05%, whereas Ni/Al_2O_3 on 304LSS thin films had an absorbance of 91.3% and an emittance of 0.15%, according to the authors' prior work [24]. The Al substrate has a more significant impact on absorbance and emittance than the 304LSS substrate.
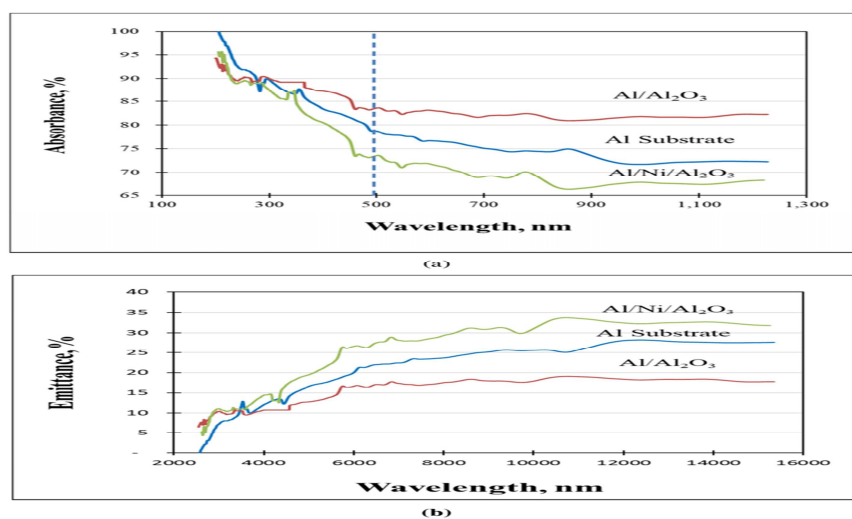

Figure 9: The Al substrate and different deposited thin films vs. wavelength in nm for (a) Absorbance percentages and (b) Emittance percentages

3.5 Nanoindentation (NIN)

The variation in NIN across coating materials may be attributable to the filler's load and composition since the coating created on the Al surface is still affected by the kind of fillers underneath. Efforts to enhance restorative materials have also concentrated on the influence of filler load on hardness [45]. The coating size and types impact the hardness and mechanical characteristics of FGNM [72, 73]. The NIN curves of Al substrate, AA-FGNM, and ANA-FGNM are shown in Fig. 10. FGNM's maximum intended depth is for ANA-FGNM coating materials. This aligns with the reduced roughness measured by AFM. Increasing the mean roughness (Ra) altered the hardness level if the indenter tip struck this region [45]. The highest nano hardness is for AA-FGNM, as shown in Table 1.
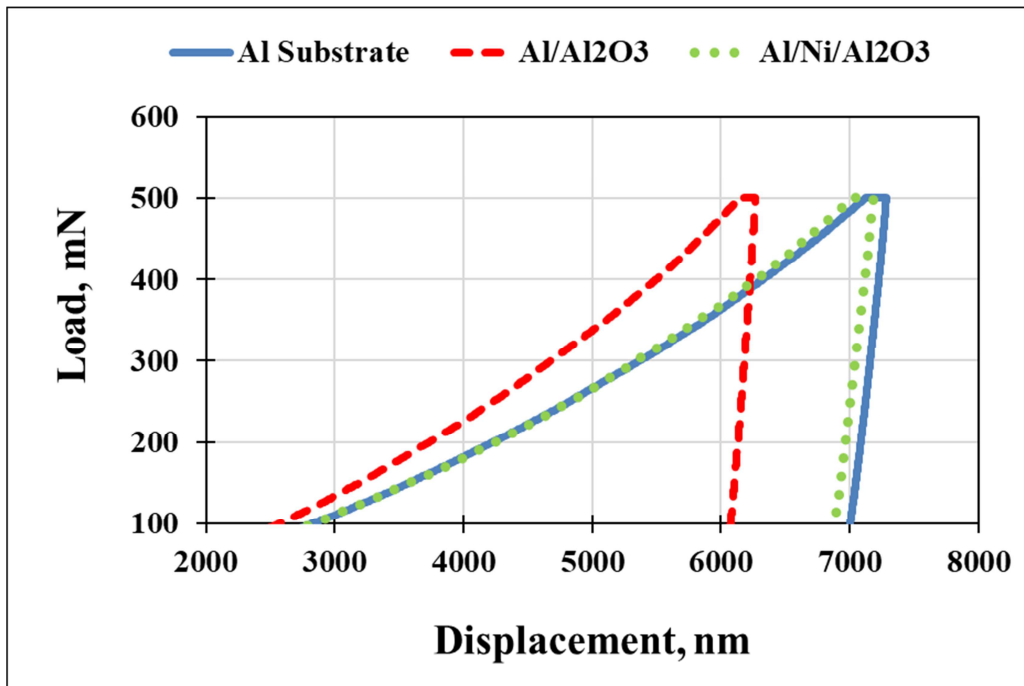

Figure 10: The NIN of Al substrate, AA-FGNM, and ANA-FGNM

Table 1: Nanoindentation test results

Conditions	Al Substrate	Al/Al$_2$O$_3$	Al/Ni/Al$_2$O$_3$
Force (max), micro-N	500	500	500
H (max), nm	7283.2	6268.4	7181.1
Hardness, N/mm^2	410	548	426

3.6 Corrosion behavior

Fig. 11 shows the layer's behavior in 3.5%NaCl at RT with a 2 mV/sec scan rate. The electrochemical parameters are recorded in Table 2. The formation of Al oxide with Ni completely changes the behavior of layers. This formation shifts the corrosion potential and current density to a negative value. There is a relation between the CRST of deposited films and the roughness. The more roughness of the surface, the less CRST of deposited layers. The deposited layer AA-FGNM has the highest CR compared with other layers due to the decreasing roughness of the surfaces. The AA has a roughness of 8.06 nm, giving a CR of 0.1 mm/y. The ANA-FGNM deposited layer has the lowest CR of 0.005 mm/y with a roughness value (2.80 nm). During film growth, the surface roughness increases due to the shadowing effect caused by the incident atoms' favored deposition on surface protrusions [70]. The combination of comparatively decreased Ra, a CRST barrier coating, and advantageous sub-surface compressive residual stresses is optimal for protecting components from corrosion and corrosion-fatigue damage [56]. The Al_2O_3 on the surface may be used in semiconductor applications due to its corrosion protection from moisture, chemicals, and other environmental factors [74]. The CR of deposited nanofilm of Al_2O_3/Ti on 316LSS in 3.5%NaCl 4.05 mm/y with a roughness of 14.41 nm before corrosion while after treatment in the furnace is 0.17 mm/y with a roughness of 6.5 nm before corrosion [75]. Thus, the corrosion characteristics of AA-FGNM are better than these results for high roughness results (8.06 nm). While the ANA-FGNM has lower roughness and CR of them thus it is suitable in marine applications due to the high CRST in NaCl.

Table 2: The electrochemical parameters of Al substrate, AA, and ANA-FGNM in 3.5%NaCl at RT

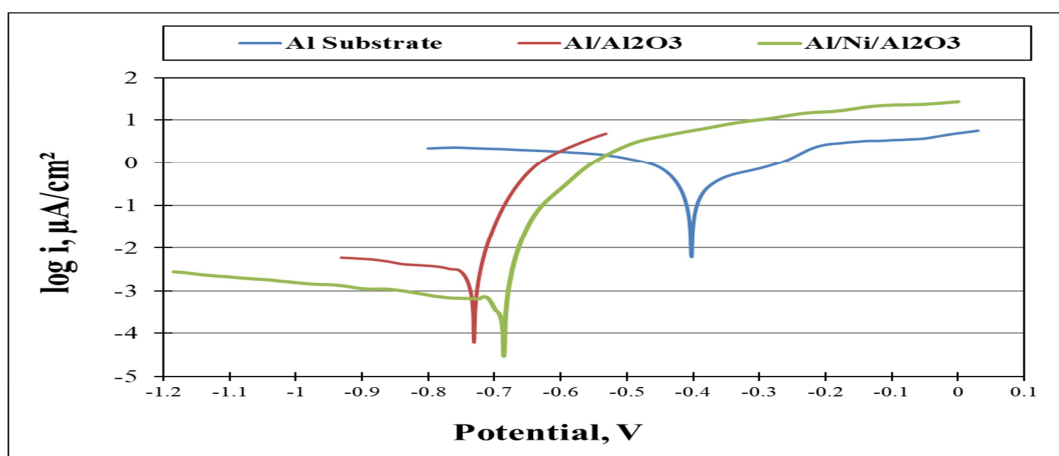| Conditions	E_{corr}, V	i_{corr}, µA/cm²	Rp, kΩ.cm²	CR, mm/Y
Al substrate	-0.4025	1.54	78.50	0.017
Al/AL$_2$O$_3$	-0.7727	0.92	9.09	0.100
Al/Ni/AL$_2$O$_3$	-0.7043	0.49	31.62	0.005

Figure 11: PDP plots of the Al substrate, AA-FGNM, and ANA-FGNM in 3.5%NaCl at RT at a scan rate of 2 mV/sec

Conclusions

The echo-environmental friendly and sustainable energy materials Al/Al$_2$O$_3$-FGNM and Al/Ni/Al$_2$O$_3$-FGNM were fabricated by sputtering on an Al substrate. The summarized characterization of them is as follows:

1. The SEM, EDX, line-EDX, and mapping of Al/Al$_2$O$_3$-FGNM and Al/Ni/Al$_2$O$_3$-FGNM have high uniform distribution with cohesive deposition.

2. The thickness coating values of Al/Al$_2$O$_3$-FGNM and Al/Ni/Al$_2$O$_3$-FGNM are almost the same, around 200 µm, while the mean roughness of Al substrate, Al/Al$_2$O$_3$-FGNM, and Al/Ni/Al$_2$O$_3$-FGNM surfaces are 1.33, 8.06, and 2.80 nm, respectively.

3. The Al$_2$O$_3$ thin film formed has spherical crystallites ranging in size from 20 nm for Al/Al$_2$O$_3$-FGNM to ~ 45 nm for Al/Ni/Al$_2$O$_3$-FGNM, as determined by XRD.

4. The contact angles for Al substrate, Al/Al$_2$O$_3$-FGNM, and Al/Ni/Al$_2$O$_3$-FGNM are 81.50°, 106.99°, and 86.10°, respectively. Al/Ni/Al$_2$O$_3$-FGNM is a hydrophilic coating, whereas Al/Al$_2$O$_3$-FGNM is a weak hydrophobic coating.

5. The nanoindentation results give a higher hardness for Al/Al$_2$O$_3$-FGNM than Al/Ni/Al$_2$O$_3$-FGNM.

6. The potentiodynamic polarization test examined in 3.5% NaCl shows that the Al/Ni/Al$_2$O$_3$-FGNM has higher CRST than Al/Al$_2$O$_3$ -FGNM, which reaches 0.005 mm/y.

7. The sustainable solar cell material Al/Al$_2$O$_3$-FGNM shows high selectivity (absorbance/emittance (α/ε)) of 0.967/0.18, compared to 0.943/0.32 for the Al/Ni/Al$_2$O$_3$-FGNM. This combination of properties makes Al/Al$_2$O$_3$-FGNM a good candidate for solar cells and mechanical applications, whereas Al/Ni/Al$_2$O$_3$-FGNM is a good candidate for marine applications.

Conflict of interest

The authors declare that they have no conflicts of interest.

References

[1]. A.A. Abbas, Z.R. Muslim, Flexural Properties of Functionally Graded Nanocomposites, Indian Journal of Natural Sciences, 9 (52) (2019).

[2]. S. K. Bohidar, R. Sharma, P.R. Mishra, Functionally graded materials: a critical review. Int J Sci Footpr, 2:18–29 (2014)

[3]. AA Kokanee, Review on functionally graded materials and various theories. Int Res J Eng Technol 4:890–893 (2017)

[4]. H. Sai B.V, A Review on Functionally Gradient Materials (FGMs) and Their Applications, International Journal of Current Engineering and Technology, 8(1), 79-83 (2018).

[5]. I.M. El-Galy, B.I. Saleh, M.H. Ahmed, Functionally graded materials classifications and development trends from industrial point of view, SN Applied Sciences, 1:1378, (2019)

[6]. B. Gupta, Few studies on biomedical applications of functionally graded material. Int J Eng Technol Sci Res IJETSR, 4:39–43 (2017)

[7]. A. Edwin, V. Anand, K. Prasanna, Sustainable development through functionally graded materials: an overview, Rasayan J Chem 10:149–152 (2017)

[8]. R.M. Mahamood, M. Shukla, S. Pityana, Functionally graded material: an overview. World Congr Eng III:2–6 (2012)

[9]. T. Taguchi, R. Tsubakiyama, K. Miyajima, Yamamoto: effect of surface treatment on photoluminescence of silicon carbide nanotubes. Appl Surf Sci. (2017)

[10]. J. Singh, A. Chauhan, Characterization of hybrid aluminum matrix composites for advanced applications—a review. Int J Mater Res Technol, (2015).

[11]. B. Saleh, J. Jiang, A. Ma, D. Song, D. Yang, Q. XU, A Review on the influence of different reinforcements on the microstructure and wear behavior of functionally graded aluminum matrix composites by centrifugal casting. Met Mater Int. (2019).

[12]. RS Parihar, SG Setti, RK Sahu, Recent advances in the manufacturing processes of functionally graded materials: a review. Sci Eng Compos Mater, (2016).

[13]. B. Kieback, A. Neubrand, H. Riedel, Processing techniques for functionally graded materials. Mater Sci Eng A. (2003)

[14]. J Rodriguez, K Hoefer, A Haelsig, P Mayr, Functionally graded SS 316L to Ni-based structures produced by 3D plasma metal deposition. Metals (Basel) 9:620 (2019)

[15]. S.A. Lajevardi, T. Shahrabi, J.A. Szpunar, Synthesis of functionally graded nano Al2O3–Ni composite coating by pulse electrodeposition. Appl Surf Sci, 279:180–188, (2013)

[16]. Muller P, Mognol P, Hascoet JY Modeling and control of a direct laser powder deposition process for Functionally graded materials (FGM) parts manufacturing. J Mater Process Technol 213:685–692. (2013)

[17]. J Song, Y. Yu, Z. Zhuang, Y. Lian, X. Liu, Y. Qi, Preparation of W–Cu functionally graded material coated with CVD–W for plasma-facing components. J Nucl Mater 442: S208–S213. (2013)

[18]. Pei Y, De Hosson JT Functionally graded materials produced by laser cladding. Acta Mater 48:2617–2624 (2000)

[19]. Del Val J, Arias-González F, Barro O, Riveiro A, Comesaña R, Penide J, Lusquiños F, Bountinguiza M, Quintero F, Pou J Functionally graded 3D structures produced by laser cladding. Procedia Manuf 13:169–176. (2017)

[20]. Yin S, Yan X, Chen C, Jenkins R, Liu M, Lupoi R Hybrid additive manufacturing of Al–Ti6Al4V functionally graded materials with selective laser melting and cold spraying. J Mater Process Technol. (2018)

[21]. Jia Q, Gu D Selective laser melting additive manufacturing of Inconel 718 superalloy parts: densification, microstructure and properties. J Alloys Compd 585:713–721. (2014)

[22]. Alimardani M, Paul C P, Toyserkani E, Khajepour A Multiphysics modelling of laser solid freeform fabrication techniques. Adv Laser Mater Process. (2010)

[23]. El-Desouky A, Kassegne SK, Moon KS, McKittrick J, Morsi K Rapid processing and characterization of micro-scale functionally graded porous materials. J Mater Process Technol 213:1251–1257. (2013)

[24]. Aliaa Abdelfatah, Lamiaa Z. Mohamed, Iman Elmahallawi, Hanan Abd El-Fattah, Comparison of structure and solar-selective absorbance properties of Al2O3 thin films with Al and Ni reflector interlayers, Chemical Papers, 2023

[25]. Y. Dou, Q. Bai, K. Yang, W. Guo, H. Wang, S. Chen, The effect of surface functional groups on the wettability of graphene oxide coated alumina substrate: Molecular dynamics simulations, Journal of Molecular Liquids 366 (2022) 120268

[26]. J. Liu, X. Zhang, R. Wang, F. Long, P. Zhao, L. Liu, A mosquito-eye-like superhydrophobic coating with super robustness against abrasion, Materials and Design 203 (2021) 109552

[27]. N. Atthi, W. Sripumkhai, P. Pattamang, O. Thongsook, R. Meananeatra, P. Saengdee, N. Ranron, A. Srihapat, J. Supadech, N. Klunngien,W. Jeamsaksiri, Superhydrophobic property enhancement on guard ring micro-patterned PDMS with simple flame treatment, Jpn. J. Appl. Phys. 59 (SI) (2020), SIIJ05, .

[28]. A.M.C. Maan, A.H. Hofman, W.M. Vos, M. Kamperman, Recent developments and practical feasibility of polymer-based antifouling coatings, Adv. Funct. Mater. 30 (2020) 1–30

[29]. W. Liu, M. Cai, X. Luo, C. Chen, R. Pan, H. Zhang, M. Zhong, Wettability transition modes of aluminum surfaces with various micro/nanostructures produced by a femtosecond laser, J. Laser Appl. 31 (2) (2019), 022503.

[30]. D. Quéré, Wetting and roughness, Annu. Rev. Mater. Res. 38 (1) (2008) 71–99.

[31]. A. Watcharenwong, N. Saijaioup, Y. Bailuang, P. Kajitvichyanukul, Morphology and wettability of nanoporous aluminium oxide film prepared by Anodization, Key Eng. Mater. 737 (2017) 174–178.

[32]. D. Zang, R. Zhu, W. Zhang, X. Yu, L. Lin, X. Guo, M. Liu, L. Jiang, Corrosion-resistant superhydrophobic coatings on Mg alloy surfaces inspired by lotus seedpod, Adv. Funct. Mater. 27 (8) (2017) 1605446.

[33]. H. Jin, X. Tian, O. Ikkala, R.H. Ras, Preservation of superhydrophobic and superoleophobic properties upon wear damage, ACS Appl. Mater. Interfaces 5 (3) (2013) 485–488.

[34]. C. Liu, L. Zhang, X. Zhang, Y. Jia, Y. Di, Z. Gan, Bioinspired free-standing onedimensional photonic crystals with Janus wettability for water quality monitoring, ACS Appl. Mater. Interfaces 12 (36) (2020) 40979–40984.

[35]. D. Wang, Q. Sun, M.J. Hokkanen, C. Zhang, F.Y. Lin, Q. Liu, S.P. Zhu, T. Zhou, Q. Chang, B. He, Q. Zhou, L. Chen, Z. Wang, R.H.A. Ras, X. Deng, Design of robust superhydrophobic surfaces, Nature 582 (7810) (2020) 55–59.

[36]. W. Lee, S.J. Park, Porous anodic aluminum oxide: anodization and templated synthesis of functional nanostructures, Chem. Rev. 114 (15) (2014) 7487–7556.

[37]. J.C. Caicedo, F. Franco, W. Aperador, Variation of adhesive stress in anodized AZ31 magnesium alloy immersed within cement concrete blocks with different solidification times, Mater. Chem. Phys. 232 (2019) 414–421.

[38]. G. Guillonneau, G. Kermouche, S. Bec, J-L. Loubet, Determination of mechanical properties by Nanoindentation independently of indentation

_____

depth measurement, J. Mater. Res., Vol. 27, No. 19, 2012

[39]. Peskersoy, C.; Culha, O. Comparative evaluation of mechanical properties of dental nanomaterials. J. Nanomater. 2017, 8, 6171578.

[40]. El-Safty, S.; Akhtar, R.; Silikas, N.; Watts, D.C. Nanomechanical properties of dental resin-composites. Dent. Mater. 2012, 28, 1292–1300.

[41]. Sauro, S.; Osorio, R.; Watson, T.F.; Toledano, M. Assessment of the quality of resin-dentin bonded interfaces: An AFM nanoindentation, muTBS and confocal ultra morphology study. Dent. Mater. 2012, 28, 622–631.

[42]. Wang, Z.; Volinsky, A.A.; Gallant, N.D. Nanoindentation study of polydimethylsiloxane elastic modulus using berkovich and flat punch tips. J. Appl. Polym. Sci. 2015, 132, 1–7.

[43]. Alrobeigy, N. Mechanical properties of contemporary resin composites determined by Nanoindentation. Tanta Dent. J. 2017, 14, 129–138.

[44]. Salerno, M.; Derchi, G.; Thorat, S.; Ceseracciu, L.; Ruffilli, R.; Barone, A.C. Surface morphology and mechanical properties of new-generation flowable resin composites for dental restoration. Dent. Mater. 2011, 27, 1221–1228.

[45]. D. Alqarni, A. Alghamdi, A. Saad, A. Ali, H. Alzahrani, K. Hosaka, Effect of Surface Polishing on Nano-Hardness and Elastic Modulus of Different Resin Composites after Immersion in Alcoholic Medium, J. Compos. Sci. 2021, 5, 327.

[46]. Bobzin, K.; Kalscheuer, C.; Carlet, M.; Schmauder, S.; Guski, V.; Verestek, W.; Tayyab, M. 3D deformation modeling of CrAlN coated tool steel compound during Nanoindentation. Surf. Coat. Technol. 453, 129148, 2023

[47]. Khan, M.K.; Hainsworth, S.V.; Fitzpatrick, M.E.; Edwards, L. A combined experimental and finite element approach for determining mechanical properties of aluminium alloys by Nanoindentation. Comput. Mater. Sci. 49, 751–760, 2010

[48]. M. Storchak, Mechanical Characteristics Generation in the Workpiece Subsurface Layers through Cutting, Crystals, 13, 761., 2023

[49]. S. Mao, H. Yang, F. Huang, T. Xie, Z. Song, Corrosion behaviour of sintered NdFeB coated with Al/Al2O3 multilayers by magnetron sputtering, Applied Surface Science 257 (2011) 3980–3984

[50]. S.E. Potts, L. Schmalz, M. Fenker, B. Dı́az, J. Światowska, V. Maurice, A. Seyeux, P. Marcus, G. Radno´czi, L. To´th, W.M.M. Kessels, Ultra-thin aluminium oxide films deposited by plasmaenhanced atomic layer deposition for corrosion protection. J. Electrochem. Soc. 158, C132–C138 (2011)

[51]. J. Masalski, J. Gluszek, J. Zabrzeski, K. Nitsch, P. Gluszek, Improvement in corrosion resistance of the 316L stainless steel by means of Al_2O_3 coatings deposited by the sol-gel method. Thin Solid Films 349, 186–190 (1999)

[52]. E. Marin, A. Lanzutti, M. Lekka, L. Guzman, W. Ensinger, L. Fedrizzi, Chemical and mechanical characterization of TiO_2/Al_2O_3 atomic layer depositions on AISI 316 L stainless steel. Surf. Coat. Technol. 211, 84–88 (2012)

[53]. R. Emmerich, B. Enders, H. Martin, F. Stippich, G.K. Wolf, P.E. Andersen, J. Ku¨delha, P. Luka´c, H. Hasuyama, Y. Shima, Corrosion protection ability of Al2O3 coatings deposited with ion beam assisted deposition. Surf. Coat. Technol. 89, 47–51 (1997)

[54]. F. Stippich, E. Vera, H. Scheerer, G.K. Wolf, X. Jian-Ming, Corrosion properties of alumina coatings on steel and aluminum deposited by ion beam assisted deposition. Surf. Coat. Technol. 98, 997–1001 (1998)

[55]. I. N. Reddy, A. Dey . N. Sridhara, S. Anoop, P. Bera, R. U. Rani, C. Anandan, A. K. Sharma, Corrosion Behaviour of Sputtered Alumina Thin Films, J. Inst. Eng. India Ser. D, 96(2), 2015

[56]. Y. Madhavi, N. Narasaiah, A. Jyothirmayi, L. R. Krishna, Influence of surface-roughness on the corrosion-fatigue behavior of MAO coated 6061-T6 Al alloy assessed in NaCl medium, Surface & Coatings Technology 414 (2021) 127102

[57]. Klocke F, Krieg T, Coated tools for metal cutting edge-features and applications. CIRP Ann Manuf Technol. 48: 515–525. 1999

[58]. Al-Rabeeah AY, Seres I, Farkas I, Selective Absorber Coatings and Technological Advancements in Performance Enhancement for Parabolic Trough Solar Collector. J Therm Sci. 2021

[59]. Panigrahi UK, Das PK, Babu PD, Mishra NC, Mallick P (2019) Structural, optical and magnetic properties of Ni− xZnxO/Ni nanocomposite, Springer Nature Switzerland AG.

[60]. Sollier E, Dunoyer N, Szambolics H, Lorin G (2017) Nanostructured thin films for solar selective absorbers and infrared selective emitters. Sol Energy Mater Sol Cells. 170: 205–210.

[61]. Zhou J, Li S, Yu Y, First principal calculation of thermal conversion properties of W-Al2O3 based solar selective absorbing coating. Comput Mater Sci. 211, 111501 (2022).

[62]. S.A.S. Asif, K.J. Wahl, and R.J. Colton: Nanoindentation and contact stiffness measurement using force modulation with a capacitive load displacement transducer. Rev. Sci. Instrum. 70, 2408–2413 (1999).

[63]. Gaber G.A., Abdelfattah A., Mohamed L.Z., A comprehensive investigation of corrosion efficiency of Cu-10Ni alloy in hybrid Cr^{3+}/Ni^{2+} with tungstate in chloride media, Egypt. J. Chem., (2024)

[64]. Petrov I, Barna P, Hultman L, Greene J, Microstructural evolution during film growth. J. Vac. Sci. Technol., A 21: S117-S128, 2003

[65]. Abouarab H, El-Mahallawi I, Kassry A, Abd El-Fattah H, Characteristics of Al & Ti oxide-thin films for thermal solar energy selective absorption applications. Mater Express. 12: 968–979, 2022

[66]. Qiang LW, Devarajan M, Variation of Structural and Surface Properties of RF Sputtered Aluminum Oxide (Al2O3) Thin Films Due to the

Influence of Annealing Temperature and Time. Int J Mater Sci Appl. 3(6): 404-409, 2014

[67]. Abd El-Fattah H, El-Mahallawi I, Shazly M, Khalifa W, Optical Properties and Microstructure of TiNxOy and TiN Thin Films before and after Annealing at Different Conditions. Coatings. 9(1), 22, 2019

[68]. Bonelli M, Guzman LA, Miotello A, Calliari L, Elena M, Ossi PM, Structure and optical properties of TiN films prepared by dc sputtering and by ion beam assisted deposition, Vacuum. 43, 5-7: 459-462, 1992

[69]. Kennedy CE, Review of Mid, to high-temperature solar selective absorber Materials. National Renewable Energy Laboratory. 520-31267, 2002

[70]. Marin E, Lanzutti A, Fedrizzi L (2013) Tribological Properties of Nanometric Atomic Layer Depositions Applied on AISI 420 Stainless Steel, Tribol. Ind. 35(3): 208-216.

[71]. Pajaczkowska PA, Reiche P, Klimm D, Majumdar G, MgO, MgAl2O4, α-al2o3, lialo2, Ligao2, NDGAO3, and SRLAGAO4: Bulk growth, Ref Module Mater Sci Mater Eng. 2017

[72]. García-Contreras R, Scougall-Vilchis R, Acosta-Torres L, Arenas-Arrocena C., García-GarduñoR, de la Fuente-Hernández J, Vickers microhardness comparison of 4 composite resins with different types of filler, J. Oral Res. 2015, 4, 313–320.

[73]. Rastelli, A.N.; Jacomassi, D.P.; Faloni, A.P.; Queiroz, T.P.; Rojas, S.S.; Bernardi, M.I.B.; Bagnato, V.S.; Hernandes, A.C. The filler content of the dental composite resins and their influence on different properties. Microsc. Res. Tech. 2012, 75, 758–765.

[74]. Lepp¨anen J., Ingman J., Peters J.-H., Hanf M., Ross R., Koopmans G., Jormanainen J., Forsstr¨om A., Ross G., Kaminski N, Vuorinen V., Aluminum corrosion in power semiconductor devices, Microelectron. Reliab. 137 (2022), 114766,

[75]. Abd El-Fattah H., Mohamed L.Z., Elmahallawi, I., Abdelfatah A., Corrosion characteristics of Ti and Al2O3/Ti thin films sputtered on 316LSS, Int. J. Electrochem. Sci. 19 (2024) 100426